FLUID STRUCTURES IN A RADIO GALAXY LOBE: OBSERVATIONS OF 3C 33 SOUTH

LAWRENCE RUDNICK
Department of Astronomy, School of Physics and Astronomy, University of Minnesota
Received 1986 March 14; accepted 1987 July 14

ABSTRACT

Models of extragalactic radio sources as interacting fluids (such as published by De Young and Axford in 1967, Scheuer in 1974, and Blandford and Rees in 1974) are supported by high dynamic range maps of the southern lobe of 3C 33. The envelope of the leading edge is similar in shape to a bow shock. Its emissivity profile is successfully modeled with equipartition particle and field pressures which scale as the fluid pressure jump across the bow shock. There is no evidence for a distinct "hot spot," such as might be expected from the jet "working surface."

In the highly detailed polarization structure behind the leading edge, we find thin curved streams, linear features at an angle to the apparent symmetry axis, and a magnetic field structure which resemble features in some numerical simulations of the leading portions of astrophysical jets (as reported by Norman *et al.* in 1985 and Woodward in 1986). Assuming a real correspondence between the observed and simulated structures, I discuss some aspects of the physics of extragalactic radio sources which might now be addressed observationally, including the relations between the synchrotron-emitting and thermal plasmas, the hydrodynamic parameters and behavior of the thermal flow, and the possible influence of the external medium.

Subject headings: hydrodynamics — radio sources: extended — radio sources: general

I. INTRODUCTION

Although detailed analyses of extragalactic radio sources are often made in the context of specific theoretical models, actual observational confirmation of these models has been hard to find. I suggest that the observations presented here may contain that type of evidence, specifically for the idea that hydrodynamic considerations govern the basic appearance and structure of the leading edges of classical double sources. Most of my discussion will focus on the numerical simulations of hydrodynamic jets, since they provide the most detail for comparison. A similar level of detail is not yet available for "blobs" or highly intermittent jets.

Initial support for the fluid beam model (Scheuer 1974; Blandford and Rees 1974) resulted, for most workers in the field, from the observations of "jets" in extragalactic radio sources (van Breugel and Miley 1977). Since that time, both observational and theoretical studies have greatly increased our knowledge of these flows, (see, e.g., the review by Bridle 1984 or the proceedings of summer workshops in Green Bank [Bridle and Eilek 1984] and in Toronto [Henriksen and Jones 1986]). In particular, numerical simulations of supersonic jet flow hold out the promise of a detailed comparison with observations, but only a few simple attempts have been made along these lines (Wilson and Scheuer 1983; Smith *et al.* 1985). Developing a detailed numerical/observation comparison is hampered by our ignorance of how the fluid parameters relate to the synchrotron emissivity, both in terms of the global scaling parameters and the more detailed structures.

While examining a gray-scale image of the southern lobe of 3C 33, I noticed what appeared to be a bow-shaped leading edge to an extended low surface brightness feature on the eastern side (see Figs. 2, 4, and 6). In an attempt to improve the signal-to-noise ratio on this (possibly symmetric) feature, I added a mirror image of the source back onto itself. Instead of an enhanced bow shock, I saw several strong diamond-shaped structures, which led me to take a closer look at similar fea-

tures in the numerical simulations. Copies of these symmetrization experiments are available in the NRAO slide collection. While it would be difficult to justify any results from such a technique, it does provide an interesting visualization tool.

II. OBSERVATIONS

The initial observations were carried out at the Very Large Array[1] on 1980 November 21. Approximately 2 hr of integration time were obtained at a wavelength of 4885 MHz, using a bandwidth of 50 MHz. Twenty-four antennas in the VLA A configuration were operational, yielding a resolution of approximately $0\rlap{.}''3$. Phase (position) and instrumental polarization calibrations were obtained using $0106+013$, with the flux density scale (Baars *et al.* 1977) and polarization position angle set by observations of 3C 286. The array phase center was at $01^h06^m12\rlap{.}^s1$, $13°02'39''$, slightly north of the southern hot spot. Therefore, only the region around this southern lobe was mapped.

A second set of observations was carried out in order to improve the signal-to-noise ratio on the interesting features which were observed. This second set took place on 1986 June 5, using 25 antennas in the A configuration, centered a couple of arcseconds from the previous observations, at $01^h06^m12\rlap{.}^s3$, $13°02'40''$, and using the same calibration sources. Observations were conducted over a period of 9 hr to obtain good visibility plane coverage, with a total integration time of ~ 5 hr (other sources were also being observed). At times, strong thunderstorms created patches of poor atmospheric phase over the site, and necessitated excision of approximately one-third of the data.

The data were self-calibrated using the algorithm of Schwab (1980). The maps displayed here, and used for self-calibration

---

[1] The Very Large Array is a facility of the National Radio Astronomy Observatory, operated by Associated Universities, Inc., under contract with the National Science Foundation.

189

were produced by CLEAN (Clark 1980), and then combined for the two observation sets. Smoothness stabilization and frequent "major" Fourier transform cycles were used to ensure good recovery of low surface brightness features. In the total intensity map, the flux of ~ 2.13 Jy was recovered by CLEAN; a linear extrapolation of the observed visibilities to zero spacing yields an estimate of ~ 2.1 Jy for the visible flux. This is not the total flux of the source (which extends over 4'), but suggests that the CLEAN map contains the flux from most or all emission which has been sampled here. The features seen in the CLEAN maps (total intensity and polarization) were robust to a number of variations in the CLEANing parameters, such as stabilization parameter, subtraction percentage, and component subtraction "boxes." Because of the self-calibration, the reader is cautioned about using absolute positions on these maps for comparison with optical or other data; the careful astrometry of Dreher and Simkin (1986) should be used for proper registration.

The above analysis and subsequent image processing were done using the NRAO AIPS software package at Minnesota using a VAX 11/780, with an FPS 5105 Array Processor and a Grinnell 512×512 12 bit image processor. Gray-scale plates in this paper were photographed directly from the Grinnell TV display screen, using transfer functions designed to enhance the features of interest.

III. RESULTS

a) Background Information

The radio source 3C 33 is associated with a DE4 galaxy (Matthews, Morgan, and Schmidt 1964) at a redshift of 0.059 (Simkin 1979). Early mapping (Hargrave and McEllin 1975) showed it to be a 250" triple (~ 200 kpc, using $H_0 = 100$ km s^{-1} Mpc^{-1}, and $q_0 = 0.5$) at a position angle of 19°. At high frequency and angular resolution, the emission is dominated by the hot spots, with small trails leading back to the nucleus; at lower frequencies and resolutions, a sinuous bridge connects the hot spots (work in preparation). Simkin (1978) tentatively identified an optical emission feature with the hot spot in the southern lobe, which was confirmed by high-resolution radio observations (Rudnick et al. 1981), and most recently, by the discovery of optical polarization matching that of the radio (Meisenheimer and Röser 1986).

b) Maps

Figure 1 is a map and Figure 2 is a plate of the total intensity of the southern lobe, using a small number of contours to mainly indicate the overall source structure. Figures 3 and 4 show the polarized intensity distribution, and Figures 5, 6, and 7a, the magnetic field orientations. The rms noise on the I, Q, and U Stokes parameter maps were 140, 51, and 47 μJy, respectively. The polarization intensities in Figure 3 are maximum likelihood estimates after correction for noise bias (AIPS program POLCOR) and are shown only when the estimated intensity was greater than 2.5 × rms noise. Figure 7a is a close-up view of the leading edge of the source, showing details of the hot spot in total intensity, and its magnetic field structure. For comparison, intensity contours for a parabolic shell are shown in Figure 7b, and are discussed further, below.

Fractional polarization values in the "hot spot" region are 30%–40%, and reach >60% along the bow-shaped feature. Even higher values, which are seen within one beamwidth of the source edge and in the low surface brightness tail, are

unreliable. Unpublished maps at 20 cm and 6 cm show that the rotation measure in the hot spot region averages approximately -7 rad m^{-2}, close to the -12 rad m^{-2} integrated value for 3C 33 (Haves 1975), so the 6 cm polarization vectors have suffered no significant rotation.

A brief summary of observed and calculated properties for several selected features is given in Table 1. These show that we are sampling regions with a range of ~ 20 in minimum pressures, from the bright peak to the diffuse region towards the northeast, assuming that they all arise in shells with thicknesses $\sim 1"$.

Gray-scale images of the total and polarized intensities and magnetic field structures are shown in Figures 2, 4, and 6. The transfer functions have been adjusted to enhance the complex structures in the low surface brightness regions. The hot spot and its "hooked" trails, which have been seen previously in polarized intensity maps, (e.g., Rudnick et al. 1981), are saturated in these pictures.

Several published displays of numerical simulation results are available for comparison with these data. The gray-scale images in Norman, Winkler, and Smarr (1983, 1984, hereafter jointly NWS) are especially useful. Full three-dimensional simulations would be preferable for comparison with the obviously nonaxisymmetric maps shown here; those simulations (e.g., Williams and Gull 1985; Arnold 1985) are unfortunately not yet of sufficient resolution.

IV. INTERPRETATIONS AND IMPLICATIONS

The aim of this discussion is to identify observed features with structures seen in the numerical simulations of astrophysical jets, and to examine what information can then be derived. In order to carry out the identification procedure, one must first decide which hydrodynamic features should be luminous. To perform a further analysis of the flow, one must also determine the angles between observed features and the local hydrodynamic flow direction. Neither set of determinations can currently be made in a complete and satisfactory way for 3C 33, or probably for any other extragalactic source. The discussion below should therefore be considered as an exercise to look at the potential of this type of analysis, and to stimulate further work.

First, I discuss the possibilities concerning the synchrotron emissivity, and their application to the interpretation of the leading edge (§ IVa). I suggest identifications for some of the other observed features in § IVb. The problem of determining the direction of flow is discussed (§ IVc), followed by an analysis demonstrating how observed features may be used to determine the physical flow parameters (§ IVd). Finally, in

TABLE 1
3C 33 South Parameters

Feature	Size/Depth[a]	Brightness (mJy arcsec^{-2})	Minimum Pressure (ergs cm^{-3})
Peak	$\sim 1" \times 1"/1"$	660 ± 2	$\sim 3 \times 10^{-10}$
Postshock	$\sim 8 \times 8 /1$	2 ± 0.5	~ 0.1
Secondary shocks[b]	$\sim 8 \times 1 /1$	$1-4 \pm 0.5$	...

[a] Each feature was assumed to arise in a thin shell. With $H_0 = 100$ km s^{-1} Mpc^{-1}, the scale is 0.8 kpc arcsec^{-1}.
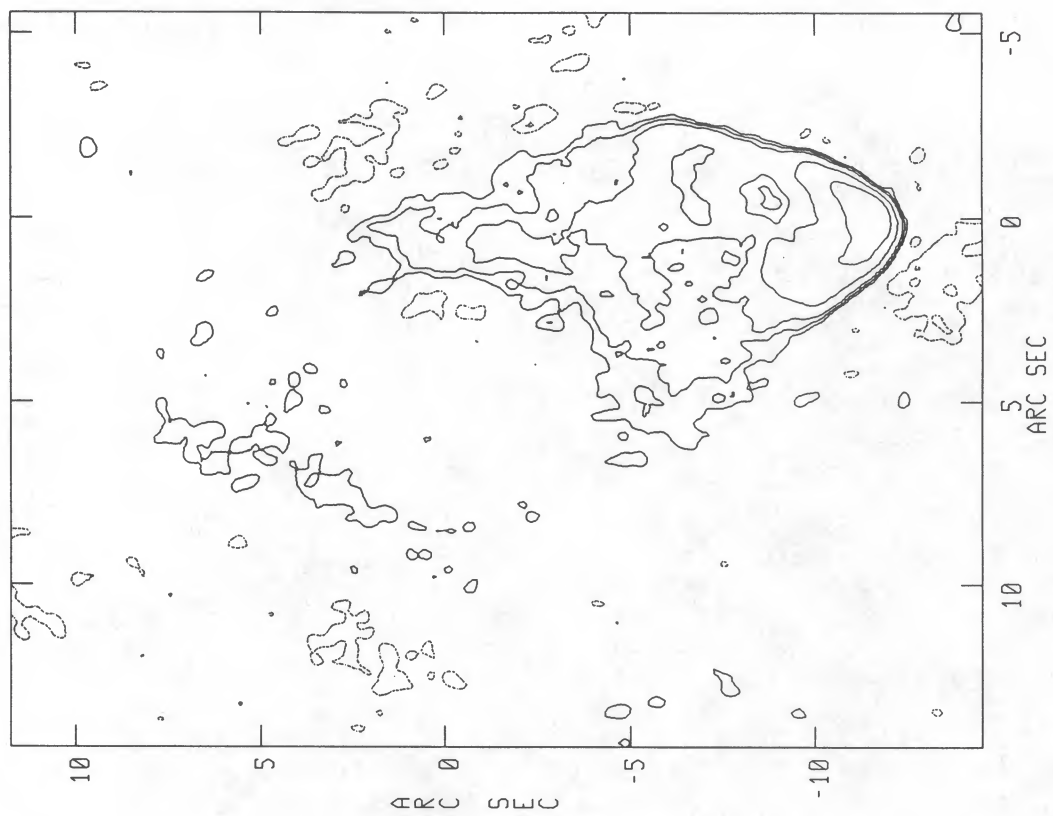[b] Polarized intensity features and values.

FIG. 2

FIG. 1.—Map of the total intensity of the southern lobe of 3C 33, with a beam size of 0″.35. Contour levels are at (1, 2, 4, 16, 64, and 256) × 0.4 mJy per beam. (0″, 0″) is at the position (01ʰ06ᵐ12ˢ1, 13°02′39″).
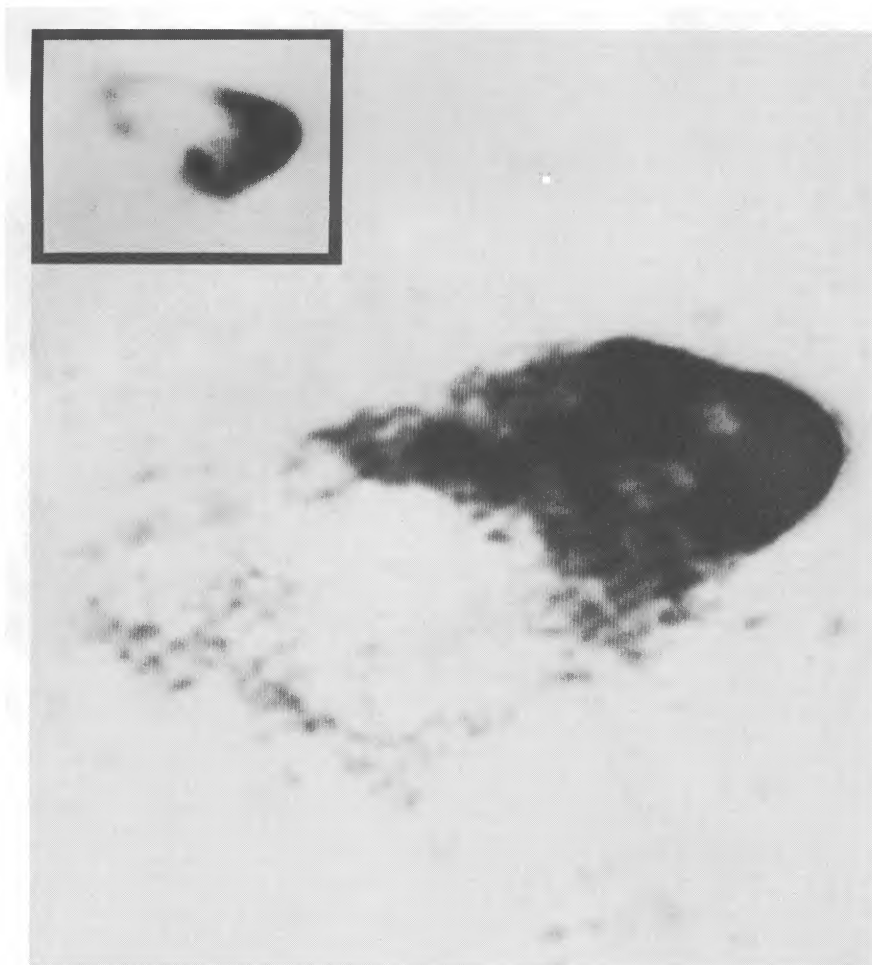FIG. 2.—Total intensity of 3C 33 South at 6 cm. The entire picture is 20″ across, and the beam size is 0″.35. The insert, with a different transfer function, shows the leading 5″.
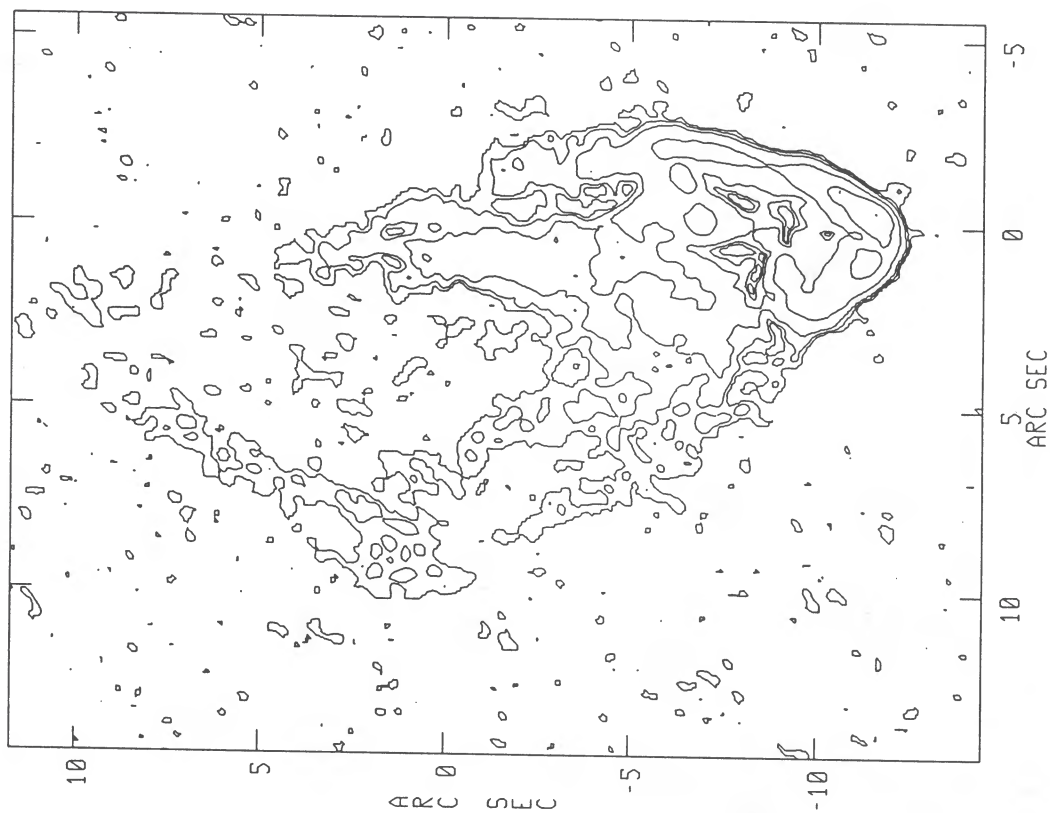
Fig. 4

ARC SEC

Fig. 3

Fig. 3.—Map of the polarized intensity, as above, and bias corrected as described in the text. Contours are at (1, 2, 4, . . .) × 0.125 mJy per beam
Fig. 4.—Polarized intensity, as above

192
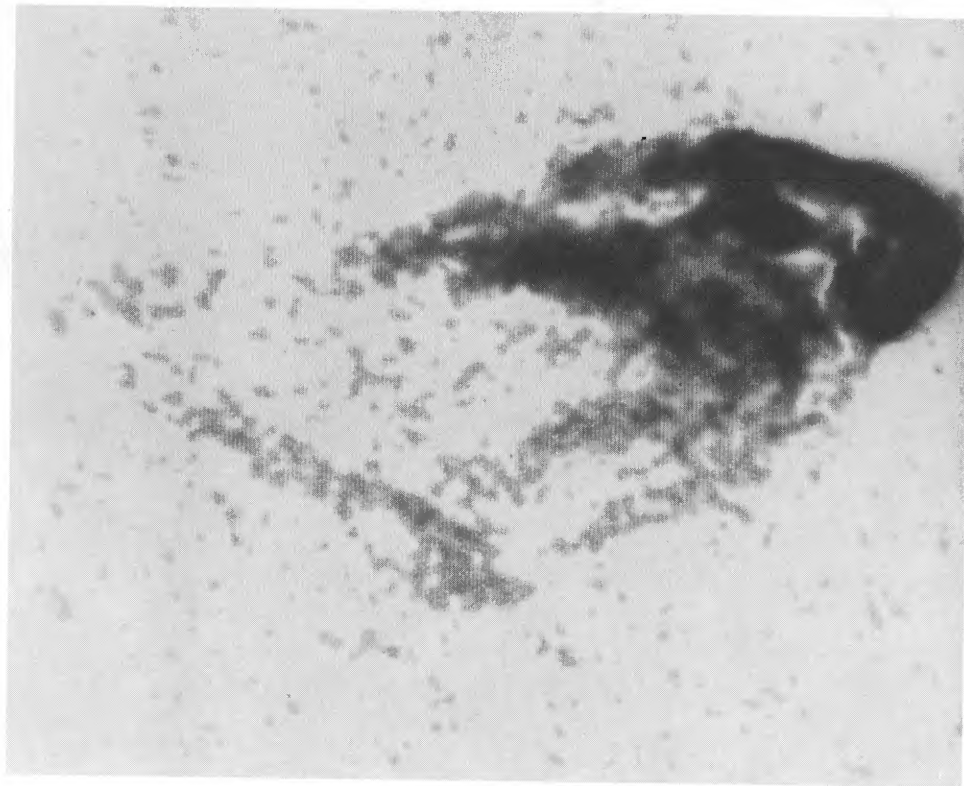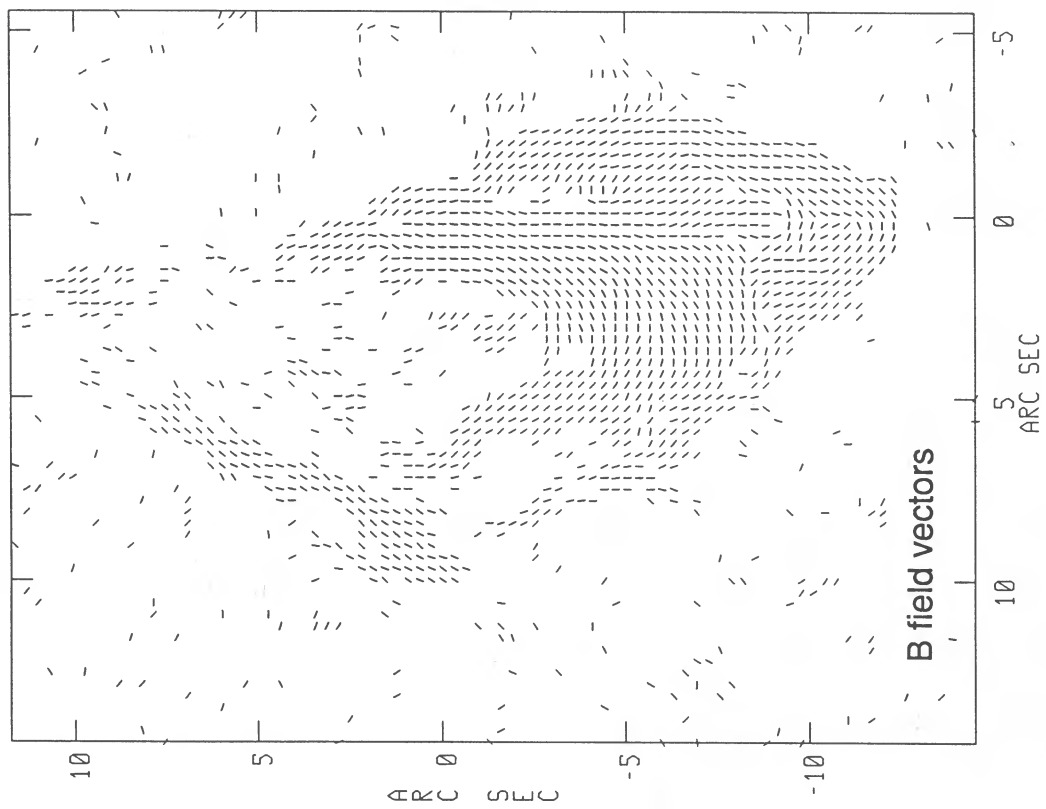
FIG. 5.—Vectors of constant length showing the direction of the *magnetic field*
FIG. 6.—Magnetic field structure. The transfer function goes nonlinearly from −90° (*white*) to +90° (*black*).
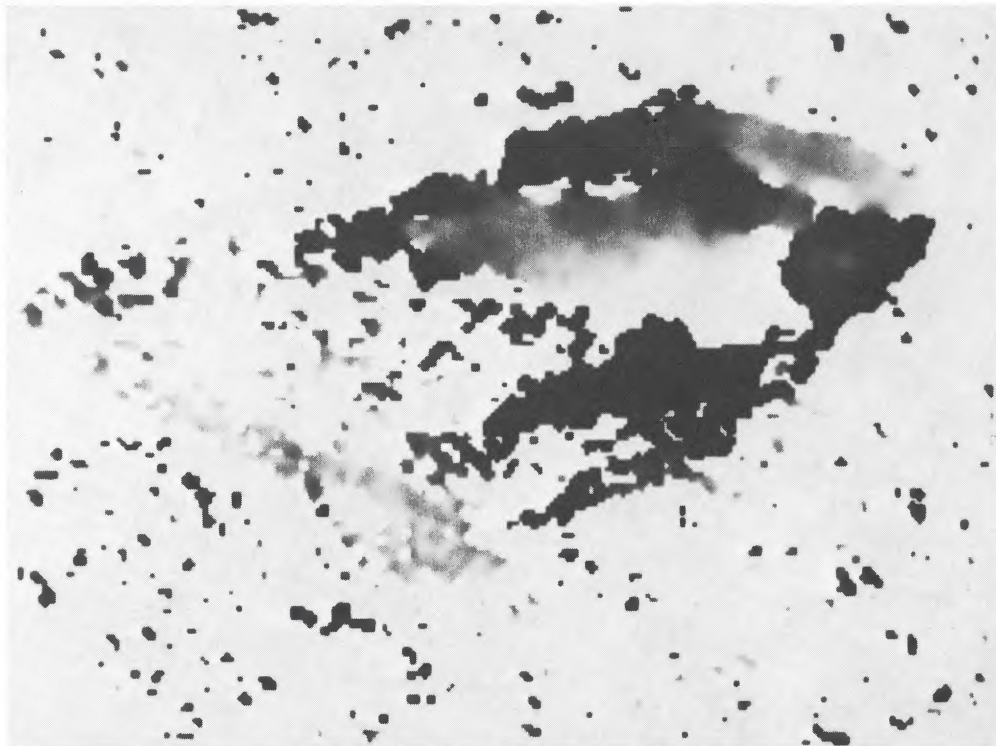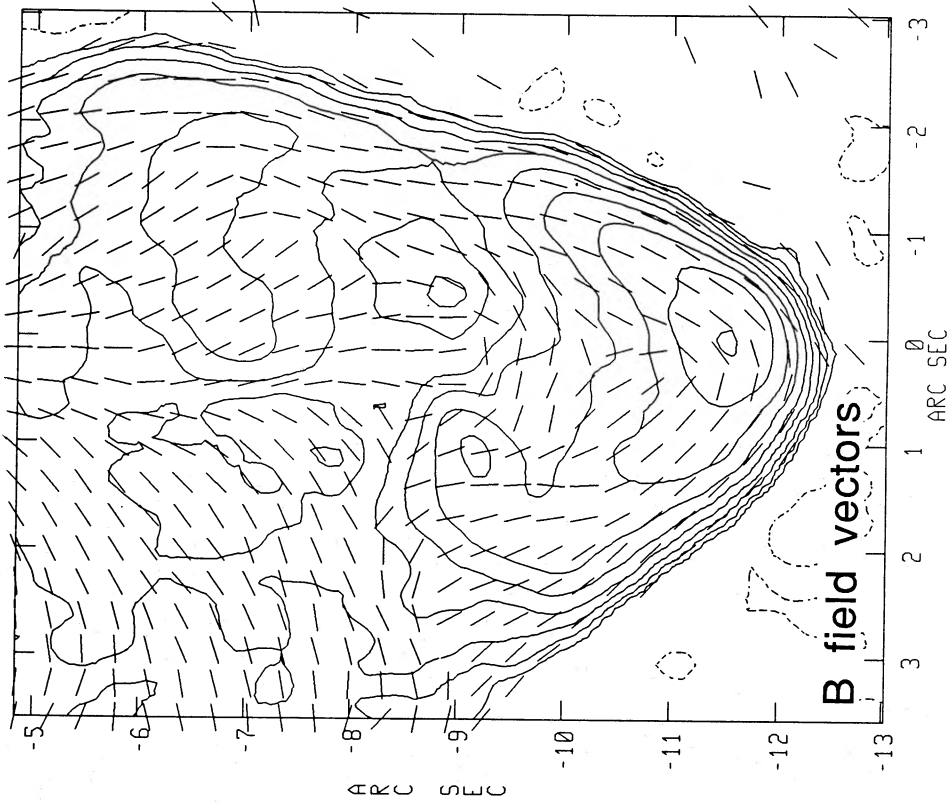
FIG. 6

FIG. 5

B field vectors

ARC SEC

193

Fig. 7.—(a) Close-up view of the leading edge, as above. Contour levels are at $(-2, -1, 1, 2, 4, \ldots) \times 0.35$ mJy per beam. Vectors of constant length again show the *magnetic field* orientations at each point. (b) Intensity contours from a thin, uniform parabolic shell, with its axis rotated by 11° from vertical. Contours are geometrically spaced by $\sqrt{2}$, starting at 1/8.33 of the peak brightness.
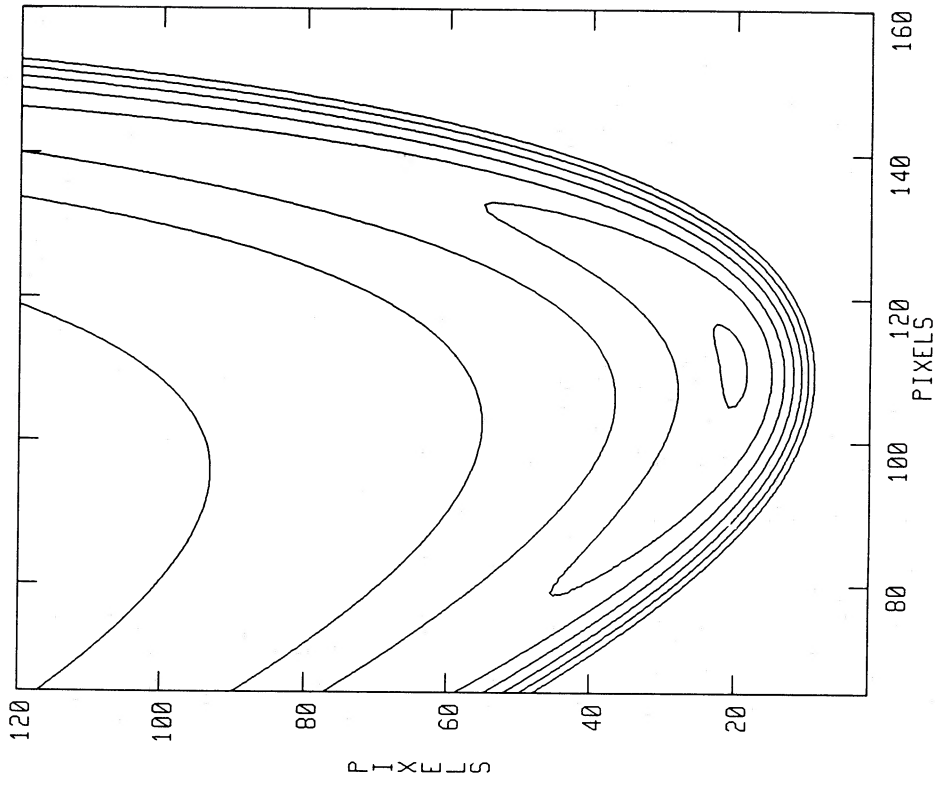
§ IV*e*, I mention the possibility of a ballistic interpretation for the observations.

The Synchrotron Emissivity
i) The General Problem

In extragalactic radio sources, we often assume that shocks, turbulence, and other hydrodynamic structures play an important role in amplifying magnetic fields and/or particle energies. However, the *origin* of the seed fields and relativistic particles is a fundamental problem which prevents us from unambiguously identifying the observed features. Several possibilities exist, within the context of the numerical simulations:

1. Relativistic particles and fields may be transported from the active nucleus to the radio lobes, where shocks, etc., increase their emissivity. Two types of structures might then be illuminated:

Supersonic jet core.—This is the region of highest relativistic particle and field density, and the strongest shocks, especially at the head.

Contact discontinuity.—Since there is also relativistic material in the backflowing cocoon, the shocks, turbulence and shear in this region may also increase the synchrotron emissivity.

2. Relativistic particles and fields may be present in the circumgalactic medium, where the bow shock and other shocks caused by the jet and cocoon will compress fields and accelerate particles.

There has so far been little to help us decide among these options. Since the nuclei are themselves sources of synchrotron emission, and since they are the source of the enormous hydrodynamic energy, it seems reasonable to assume that the relativistic particles should exist at least within the contact discontinuity. Smith *et al.* (1985) in their modeling of hot spots, have assumed that no synchrotron emission comes from outside the contact discontinuity and attempted to justify this on the basis of intergalactic magnetic field limits.[2]

At present it seems wise to consider the possibility of emission from both inside and outside the contact discontinuity. From radio, X-ray, and emission-line studies, we know that there are large amounts of relativistic and hot and cold ($\sim 10^4$ K) gas outside of galaxies (Noordam and de Bruyn 1982; Canizares 1987; van Breugel 1986). From Faraday rotation studies (see Laing 1984), we know that magnetic fields, mixed with thermal particles, are found outside of the strong emission regions. From the decade it took extragalactic astronomers to find jets, we know that they can often carry substantial amounts of energy with a very low synchrotron emissivity. In this discussion, I will therefore consider features for identification both inside and outside the contact discontinuity.

There is a second question regarding the synchrotron emissivity, which can be considered somewhat in parallel; viz., is there local particle acceleration where the source brightens? Alternatives to particle acceleration include simple compression of the magnetic fields and relativistic plasma, or the scattering of relativistic particles into radiative orbits around the magnetic field lines.

ii) The Leading Edge

With the dynamic range of over 500:1 (peak:rms) a basically parabolic shape outlines a bright leading edge, extending into a low surface brightness (1–10 mJy arcsec^{-2}) region (Fig. 2). The shape of the highest contours are similar to those expected from a parabolic shell (see Fig. 7*b*), but the observed decline in brightness from the peak is much too steep, if the shell had a uniform emissivity.

To examine the falloff in emissivity more closely, I measured the brightness as a function of position along the leading edge, as follows. (Readers may wish to skip to the results in the next paragraph.) Using a map rotated by 11°, I first drew a freehand curve which traced the western boundary of the leading edge. (I did not use the eastern boundary, because it terminated so quickly.) I then measured over 50 positions along the curve to allow a fit to its shape. A second-degree polynomial was fitted to the curve, yielding residuals of approximately 0″022 (including a first-order term, which corrected for my imperfect map rotation). The remarkable accuracy of this parabolic fit may be verified by overlaying Figures 7*a* and 7*b*. It is aided, on short spatial scales, by my freehand smoothing over irregularities which were smaller than the beam. A fourth-degree polynomial[3] yielded a somewhat better fit (residuals $\sim 0″015$) and was used in the subsequent analysis. Local values of the slope were calculated from the analytic derivative of the polynomial. I then slid the drawn curve toward the NE, until it overlaid the locus of maximum brightness along the edge. I measured the crossing positions of total intensity contours spaced at successive factors of $\sqrt{2}$ in brightness, until they reached a local minimum approximately 3″5 from the peak.

The falloff in brightness with position along the leading edge was examined by plotting the observed intensities at each contour crossing versus various functions of position. Approximately 10 independent beam areas are represented. One function of position,[4] (M_{perp}/M_0), is a measure of the projection of the symmetry axis vector along the direction perpendicular to the curve, at each position. A linear fit to the [ln (brightness) vs. ln (M_{perp}/M_0)] data yields a slope of 4.3 (see Fig. 8), and a residual of 0.13 in ln (brightness), or $\sim 14\%$. I then estimated the *emissivity* at each point by dividing the observations by the brightness of a thin uniformly emitting parabolic shell, as shown in Figure 7*b*. The slope of the [ln (emissivity) vs. ln (M_{perp}/M_0)] line is 3.7 ± 0.18.

If we interpret the leading edge as a bow shock, $(M_{perp}/M_0)^2$ is an approximate measure of the pressure ratio across the shock. The emissivity then falls off slightly slower than the square of the pressure (p^2 was assumed by NWS in their hot spot simulations).

How do we expect the emissivity to scale with pressure? Making the simplest possible assumption, that the equipartition pressure of the relativistic particles and fields scales with the fluid pressure behind the shock, leads to the relation:

$$\text{emissivity} \propto (\text{pressure})^{1.75} \qquad (1)$$

The observed relation is:

$$\text{emissivity} \propto (\text{pressure})^{1.86 \pm 0.09} \qquad (2)$$

---

[2] Ruzmaikin and Sokoloff (1977) derived an upper limit of 10^{-10} G for any intergalactic magnetic field. However, that derived limit is of little use in the current context, because it applies to a mean intergalactic field (that is, the vector average along the line of sight to quasars), and not to the possibly stronger fields in the environs of individual galaxies.

[3] There is no "standard" shape for bow shocks, and the analytic approximations by DeYoung and Axford (1967) and Raga (1986) contain significant terms at least to fourth order.

[4] Other functions also provided comparably good fits to the brightness falloff, including [ln (brightness) vs. (distance along curve)] or [ln (brightness) vs. (M_0/M_{perp})]. I have chosen to discuss the function in the text, because of its physical significance.
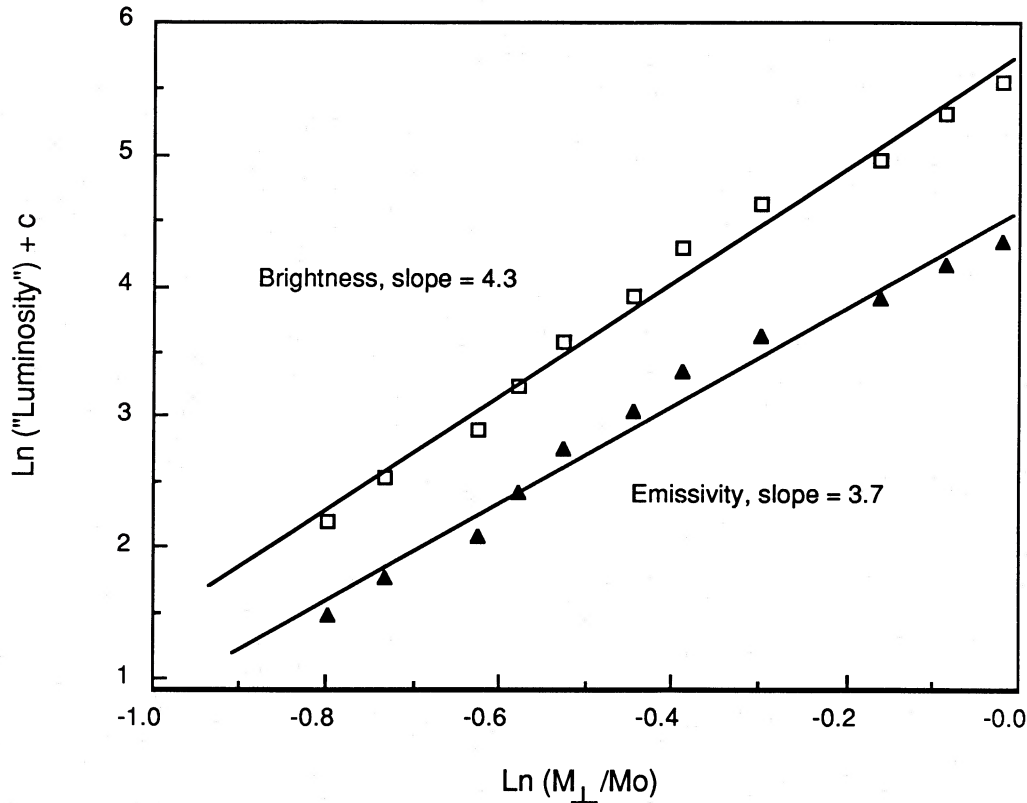
FIG. 8.—Plot of brightness and emissivity along the western leading edge of 3C 33 South, as a function of the local inferred perpendicular Mach number (see text)

This strongly suggests that (*a*) the shock jump relations are a good description of the conditions at the leading edge, and (*b*) *the leading edge is in equipartition between relativistic particles and fields.* This is the first demonstration of a scaling behavior in extragalactic radio sources which shows an equipartition signature.

If the preshock material had simply been compressed adiabatically, applying the normal shock jump conditions, and assuming $\gamma_{rel} \propto T_{thermal}$, its emissivity $(n_{rel}\gamma_{rel}^2 B^2)$ would scale as $\sim(\text{pressure})^{2.5}$ for Mach numbers from 1 to 2.5. (For strong shocks, the scaling changes to $[\text{pressure}]^2$.) This analysis assumes that B is primarily perpendicular to the local shock velocity, as is observed. The 2.5 power-law index is not well matched to the observations, so the equipartition explanation seems more appropriate.

A further result of this analysis is that there is *no distinct hot spot*, i.e., the bright region, with a power-law shape, has no characteristic size. A scale is eventually forced on the system only by the linear "hooks" that extend from the east and western borders. The shape of the leading edge, the lack of a distinct hot spot, and the equipartition-scaled smooth variation of emissivity along the edge all provide support for the bow shock interpretation. Structures such as this are seen rarely, if at all, within the contact discontinuity (Smith *et al.* 1985).

The full opening angle of the inferred bow shock is $\approx 51°$, corresponding to a Mach number of 2.3 for the advance of the jet into the external medium (M_{head}). Note that the opening angles in the numerical simulations of NWS are much wider than expected from their corresponding external Mach numbers. This is due to the influence of the uneven radial

zones, and only structures within the uniformly gridded area are reliable (M. L. Norman, private communication).

The actual Mach number could be much higher than the value of 2.3 inferred, above, if we are only seeing the very front of the bow shock. The reader should be aware of this caveat to the discussion.

If the bow shock were nonradiative, and simply compressing the particles and field, the maximum increase in emissivity would only be a factor of 100 over the background (for $M = 2.3$). If such a background were to exist over a cylinder 200 kpc long and 5 kpc in diameter, its emissivity would have to be at least 1000 times lower than the leading edge, to avoid doubling the total flux of the source (a very conservative limit). It thus appears unlikely that simple compression can illuminate the leading edge. The localized particle acceleration which is needed for the optical emission is probably also required for the radio emission. Particle acceleration in supernova shocks has been discussed for a decade (Bell 1978; Blandford and Ostriker 1978), but little work exists on possible extragalactic applications. In a recent analysis of the apparent bow shock in NGC 1068, Wilson and Ulvestad (1987) also found a need for very high compression ratios; they preferred an explanation in terms of a radiatively cooling shock.

All of this analysis assumes that the relativistic particle pressure is small. However, the apparent equipartition behavior of the accelerated particles suggests that they may also be regulating the shock structure itself.

The gray-scale image of the leading edge (see Fig. 2 [*insert*]) bears a striking resemblance to the [S II] image of HH 34 (Reipurth *et al.* 1986), including a "hook" extending from the leading edge. Radiative bow shock models of Herbig-Haro

objects have also been studied for a number of years (see Schwartz 1983).

b) Identification of Other Fluid Features

Four major aspects of these images suggest analogies to laboratory jets and the numerical simulations of astrophysical jets. These are the leading edge, interpreted above as a bow shock; curved filamentary structures (secondary shocks?); linear features at an angle to the apparent source axis (oblique shocks?); and the magnetic field configuration, suggesting an orderly flow. Figure 9 is a schematic of the polarization map, indicating these features, which are discussed below.

This paper represents a first attempt at identifying such structures and is necessarily speculative.

i) Curved Features

In contrast to the total intensity appearance, the polarized intensity map (Fig. 4) has a very detailed structure, when examined at low surface brightness levels. These same structures might also be present in total intensity, but with too low a contrast to be isolated in the current data. The low surface brightness region, extending 15″ NE of the bright leading edge, is threaded by a number of filamentary structures, some straight and some curved.

Although the curved structures are often interrupted by others, several of them appear as faint images of the leading edge. These are identified as "secondary shocks" in Figure 9 and have opening angles in the range of 50°–60°. They each have bright patches near their southern edge; the locus of these bright patches form an irregular band of polarized emission at an angle of ~20°, which might trace the path of the advancing beam.

The curved features range in brightness from ~0.15 mJy per beam, where they fade into the diffuse structure, to ~0.5 mJy per beam, where they appear at a factor of 2 contrast. There are only minor changes in the field directions as one crosses the curved features; they are therefore probably best understood as enhanced portions of a well-ordered flow region behind the leading shock. In fact, the diffuse emission could be merely a superposition of the lower brightness tails of the curves which we see.

At present, it is impossible to determine whether these curved structures are within the outflowing jet core, the back-flowing cocoon, or the shocked external medium. Such secondary shocks can be formed at triple points from internal shocks or could result from instabilities which cause the beam to advance in intermittent spurts. If we could specify the appropriate location for these shocks, we could use their opening angles to determine the local flow conditions, such as discussed below.
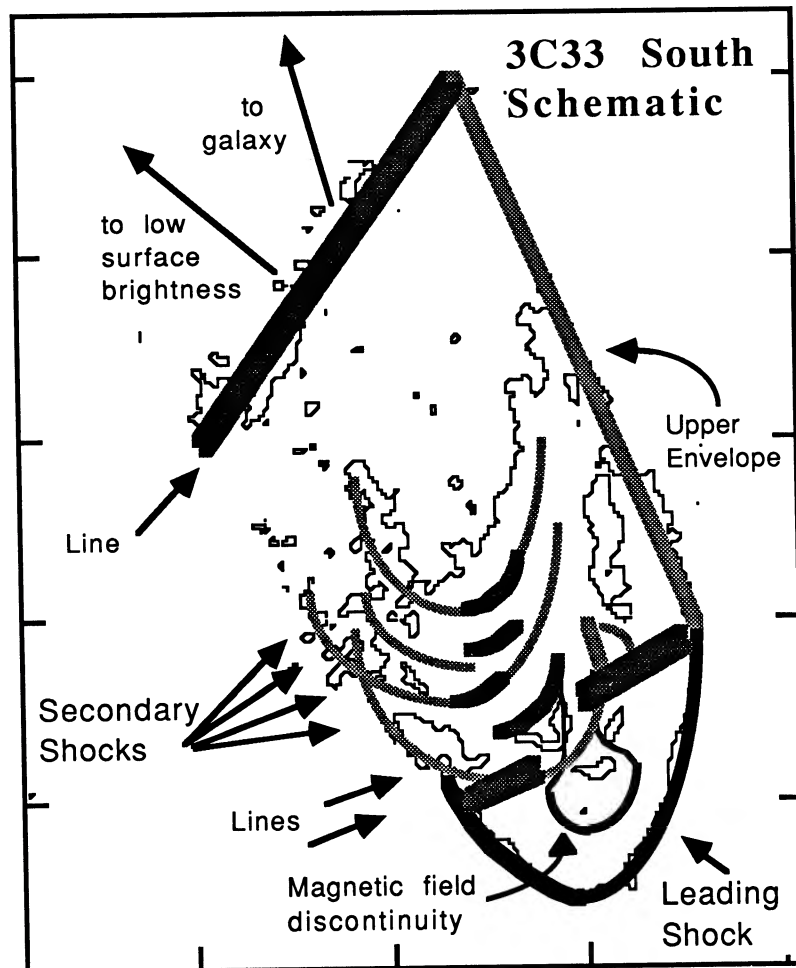

FIG. 9.—Schematic diagram of the polarization structures

ii) *Lines*

Linear features are visible in the polarized intensity map. The brightest of these is the western "hook" which appears to terminate the bright leading edge, and is also seen in total intensity. It is modulated in brightness by three "components," whose structure is not well resolved, and may be related to the superposition of other features within the diffuse background. This also confuses the interpretation of its magnetic field structure, which, although ordered, bears no obvious relation in orientation to the structure. A similar, shorter line terminates the leading edge on the eastern side.

At the NE extremity of the diffuse emission region, a resolved linear feature ($\sim 12''6 \times 2''$) is seen both in total and polarized flux. Its magnetic field lies along the structure.

North of the bright leading regions, patchy lines are seen as the upper (NW) envelope of diffuse emission (see Figs. 4 and 9), and as a band which leads from the western "hook" until it intersects the upper envelope. Together, these lines and the superposed emission from the western portions of the curved features form a triangular-shaped region.

In the numerical simulations, lines of high density and/or pressure are seen where oblique shocks develop within the beam. These oblique shocks can form with "odd" symmetry around the flow axis (e.g., in helical modes), or with even symmetry, in which case they appear as diamonds. Such shock diamonds are seen in jet aircraft exhausts (see Norman and Winkler 1985, or the spaceflight movie "The Dream is Alive") and also appear in symmetrized simulations.

Linear features are most easily produced within the outflowing jet, and the analysis below assumes that location for the observed "lines" in 3C 33. This interpretation is not completely self-consistent, because the leading bow shock should then appear much larger than it does.

iii) *Magnetic Field*

Magnetic field directions are commonly interpreted as indicating the local directions of fluid shear (parallel to B) or the existence of compression (transverse to B). At the leading edge of 3C 33's southern hot spot (Fig. 7a), the magnetic field lines run parallel to the brightness contours. Such circumferential fields have been recognized for a long time (Fomalont 1972) and could indicate either the compressed interface with the ambient medium or the local shear.

Along a roughly north-south axis, the magnetic field vectors are almost completely aligned (Fig. 5), similar to the parallel B fields of strong radio jets (e.g., Bridle 1982). This parallel field axis is probably spatially unresolved in the current observations and might be identified with the incident beam. Away from the axis polarization remains high, and the field direction slowly curves away, in a symmetric pattern (Fig. 5). On the eastern side, the magnetic field directions closely parallel those of the curved "secondary shocks," but no corresponding features are visible to the west of this axis.

Just before reaching the hot spot, the magnetic field along the axis flips to the transverse direction. It then curls back to merge with the larger scale pattern, as if it were itself the terminus of a flow, *behind* the leading edge. This behavior is most clearly seen in Figure 7a, which is the expanded version of the head of the source. Curiously, this clear field transition occurs in a region of *low* polarized and total intensities. If the incident flow has actually been terminated at this point, with the field orientation flips showing the contact discontinuity (see Fig. 6),

then the brightest part of the source would be located outside, in the shocked external medium.

c) *Complications to the Analysis*
i) *Determining the Local Flow Direction*

The analysis of hydrodynamic flow parameters (see § IV*d*) relies on measuring the angle between the flow and any shocks or other observed features. At this time, it is not possible to uniquely define the flow direction in the southern lobe of 3C 33. There are several "suggestive" directions, as follows (angles quoted below refer to the direction from which the flow appears to come, in degrees east from north):

1. *Toward the nucleus (19°).*—This "natural" direction is also indicated by the upper envelope of emission ($23° \pm 2°$) and the steepest gradient of the hot spot seen in high resolution 2 cm observations ($20° \pm 4°$, in preparation).

2. *Symmetry axis for the leading edge ($11° \pm 2°$).*—I determined this axis by making a transport overlay of a total intensity contour map, flipped it over, and rotated it until there was a good match between the two images (see Fig. 10).

3. *Toward the low surface brightness emission.*—Low-resolution observations of the bridge between the nucleus and lobes (work in progress) show it to have a sinuous shape in both the north and south. The emission immediately north of the bright southern lobe is located at a position angle of $50° \pm 3°$ from the hot spot. If this low surface brightness emission represents the flow path, then defining a local direction may depend on making a model of its full sinusoidal locus.

4. Examination of the magnetic field orientation map, Figure 5 (and Fig. 6), suggests yet another important direction, $0°$. For a distance of approximately 10", the magnetic field is aligned along a straight line, at a position angle of $0° \pm 3°$ which terminates in a transverse field region, just behind the bright leading edge. This line is somewhat interrupted by the "hook" at the northwest end of the high surface brightness edge. The magnetic field "line" has no obvious counterpart in either the polarization or total intensity maps.

Physically, the existence of several characteristic directions implies the existence of several dynamically important factors. These might include the initial beam direction, pressure gradients, winds, or clouds in the external medium, or accelerated motion or precession of the nucleus.

ii) *Projection Effects*

These can further complicate the analysis, by distorting shapes or angles. For the purposes of this discussion, I will assume that all features are either figures of revolution around the local flow axis, or planes (which, strictly, are not allowed in the symmetric two-dimensional simulations). Using this assumption, we can attempt to estimate the angle between the flow axis and the plane of the sky.

The major effect of project is to increase the observed opening angle of the leading edge. The Mach number discussed for the leading edge must therefore be considered as a lower limit.

The parabolic shaped boundary of the leading edge does not allow us to use its "softness" as a measure of projection. In any projection, the brightness profile along the symmetry axis of a parabolic shell maintains the same shape and distance scale; only the path length through the shell, or brightness, changes its normalization as the line of sight changes angle with respect to the flow direction.

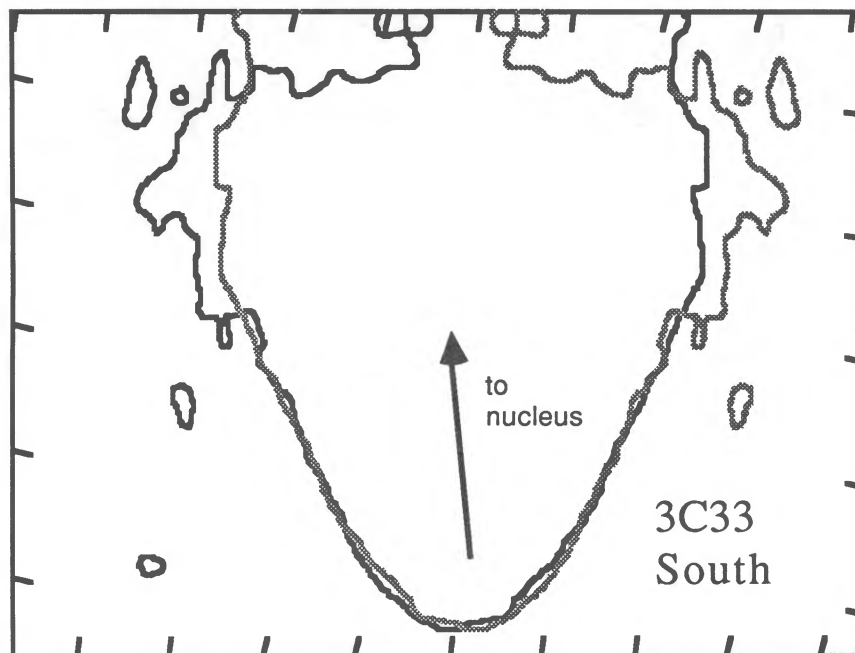One feature is useful for estimating projection effects—the

FIG. 10.—Plot of a single total intensity contour, rotated through an angle of 11° (*black* line) and then reflected about the new vertical axis (*gray line*). The direction to the nucleus in the black frame is also shown.

"line" which forms the northeast terminus of the southern lobe. I convolved the map along this line, to a resolution of $12\rlap{.}''6 \times 0\rlap{.}''5$, to increase the signal-to-noise ratio, and then measured its width as $2''$, full width at quarter-maximum. This includes any contribution from the features' nonlinearity. If the feature is basically planar, this sets a limit of $\sim 9°$ on the projection angle.

Based on these results, I have ignored any complications from projection effects in the following discussion.

d) Derivation of Fluid Flow Parameters

In most of the numerical simulations that have been performed to date, two important restrictions are used to reduce the investigated parameter space. First, static pressure balance is presumed to hold between the jet and external fluids. Second, there are no natural scales in the system,[5] and results can be expressed, e.g., in units of the external density, sound speed, and the sound crossing time for the beam radius. Within these restrictions there remain only two free parameters, which are commonly taken as the density ratio between the beam and external media ($\rho \equiv \rho_b / \rho_m$), and the Mach number of the incident flow, M_b (i.e., with respect to its own sound speed).

The determination of the Mach number of the advance of 3C 33 into the external medium (M_{head}, as discussed above, with respect to the sound speed of the external medium, c_m), can be used to pin down one free parameter. Although the observational situation is not clean at present, I will here identify the *lines* in 3C 33's polarization structure as internal shocks and illustrate how these may be used to fix the second free parameter. Then, within the limits of the numerical simulations themselves, the physical characteristics of the fluid flow can be determined.

The angle made by the shocks with respect to the flow axis (which we assume here that we can measure) is dependent on the Mach number with which the shocks themselves move through the beam fluid (i.e., the *pattern* speed), so

$$\sin (\theta_{\text{shock}}) = 1/M_{\text{shock}} , \qquad (3)$$

where M_{shock} is taken with respect to the sound speed of the beam fluid, c_b. To combine the information from our derived M_{head} and M_{shock}, we then need to set up two frames of reference, a wave frame in which the shock patterns are at rest, and an *observer* frame, in which the parent galaxy and external medium are assumed to be at rest. The velocities of interest in the two frames are defined in Table 2.

Empirically, one often finds that the frame in which the waves are at rest is determined by the balance of the momentum density (or mass flux) between the jet and (incoming) external medium (P. R. Woodward, private communication). That is,

$$\rho_b u_b{}^w = \rho_m u_m{}^w , \qquad (4)$$

where u^w represents the velocity (beam or medium) in the rest frame of the shock wave. For the NWS simulations, this relationship is verified in a somewhat indirect form, as follows: Using the known density ratio ρ and the incident jet Mach number, equation (4) can be used to predict the Mach number

---

[5] Such an assumption might be violated, for example, if synchrotron energy losses were dynamically important (Eilek 1979), imposing an external time scale on the system.

TABLE 2

DEFINITION OF REFERENCE FRAME VELOCITIES[a]

Reference Frame	Shock Pattern	Incident Fluid	Head	External Medium
Wave	0	$u_b{}^w$	...	$u_m{}^w$
Observer	...	u_b	u_{head}	0

[a] I have included only entries for variables which are used in the text.
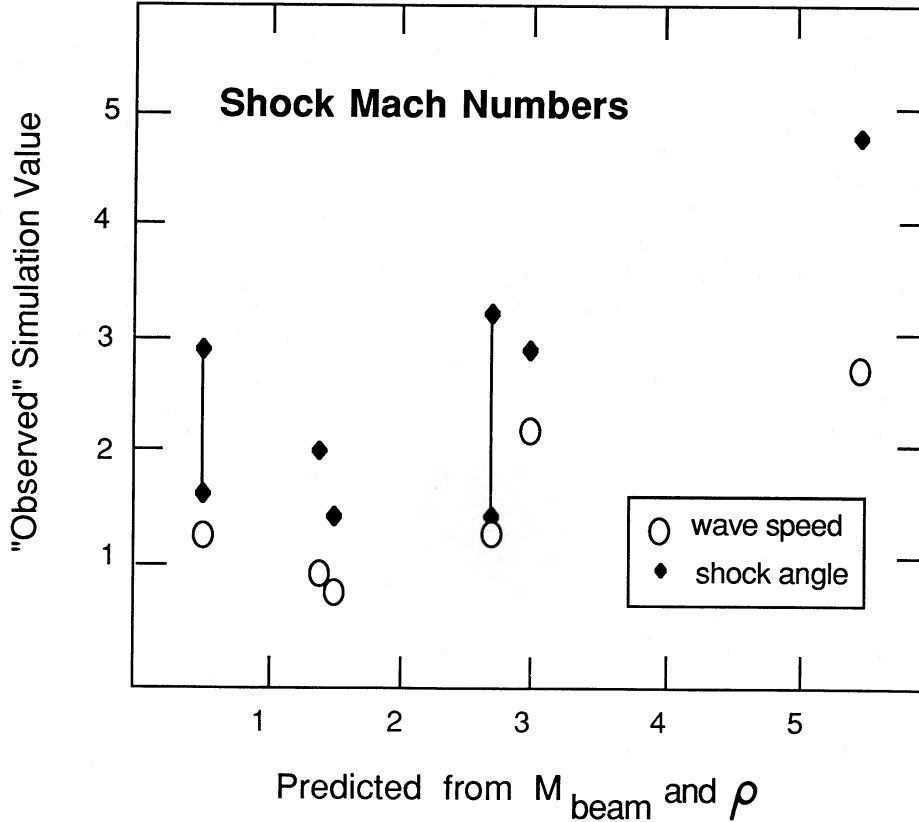
Fig. 11.—Comparison of "predicted" and "observed" shock Mach numbers for NWS simulations, to test validity of eq. (4). See text.

of the shock pattern (in their own rest frame). These predictions are compared in Figure 11 to the shock Mach numbers "observed" in the NWS simulations, both by looking at the angles of the shock lines to the flow (eq. [3]), and from the space-time plots. These comparisons show that equation (4) is sometimes a useful approximation, although caution is warranted.

We make a further connection between the incoming fluid flow and the advance of the head by the common ram pressure condition,

$$\rho_m u_{\text{head}}^2 = \rho_b (u_b - u_{\text{head}})^2 . \tag{5}$$

Using equations (4) and (5) and the static pressure balance condition elsewhere along the jet,

$$\rho_b c_b^2 = \rho_m c_m^2 , \tag{6}$$

we find that

$$\mu \equiv (M_{\text{head}}/M_{\text{shock}}) = (1 + \rho)/(1 + \sqrt{\rho}) , \tag{7}$$

where $\rho = (\rho_b/\rho_m)$. If we generalize this to account for the *efficiency* (ϵ) of the beam in transferring its momentum to the advancing head, then we must write

$$\mu/\epsilon = (1 + \rho)/(1 + \sqrt{\rho}) , \tag{8}$$

where $\epsilon \equiv$ (true head advance speed)/u_{head}. In the parameter range explored by NWS, a typical $\epsilon \approx 70\%$ was found.

A plot of μ/ϵ as a function of ρ is found in Figure 12. It shows that this total procedure is of limited usefulness, because μ/ϵ takes on values near unity for a wide range of ρ's; only ρ's significantly greater than unity can be isolated.

Since all parameters are known for the simulations, they can be used as a consistency test of the above procedure. The results of two such tests are shown in Figure 13, where the actual density ratios, ρ, are compared with ratios derived from equation (7). The squares result from *assuming* that M_{head} was equal to the u_{av} measured from the simulations, and deriving M_{shock} from equation (4). This procedure leads to reasonable estimates of the actual value of ρ, but depends on knowing u_{av}, which is not directly observable. When I use only the observable shock angles, internal and leading external, the predictions for ρ (plotted as circles) are not good. This whole analysis should only be understood as an illustration of a potentially useful tool. A much fuller understanding of the connection between observable quantities and flow physical conditions will be necessary for this tool to be productive.

In the case of 3C 33, I estimated that the shock angles were between 45° and 75°, using the "lines" indicated in Figure 9 and an 11° angle for the incident flow. Using this range of values, μ would fall between 1.6 and 2.2. Assuming $\epsilon = 70\%$ leads to a range of $5 < \rho < 10$. The beam thus appears to be "heavy" because the internal Mach numbers are lower than the external one. At present, this result should be treated with great caution.

The above analysis has been based on symmetric simulations, while the features observed in 3C 33 do not share this symmetry. Full three dimensional simulations, such as those by Arnold (1985), show that small-scale fluid density asymmetries of order 10 occur spontaneously within the cocoon even at low resolution. Further work may show whether these spontaneous 3-d asymmetries are sufficient to explain the observed asymmetric details. Alternatively, the complications of
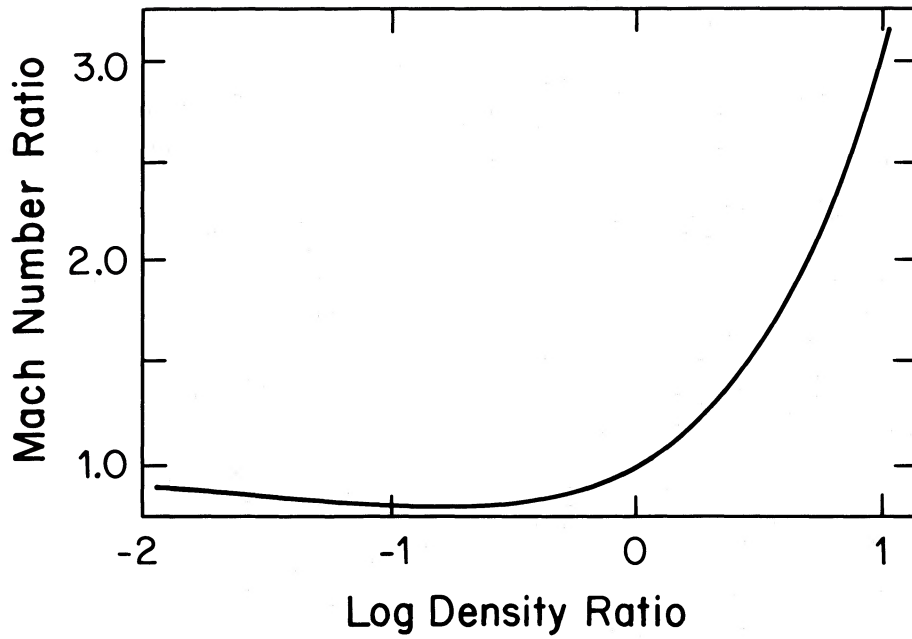
FIG. 12.—Predicted dependence of the observable ratio of shock and head advance Mach numbers on the density ratio between the beam and ambient medium (eq. [9]).
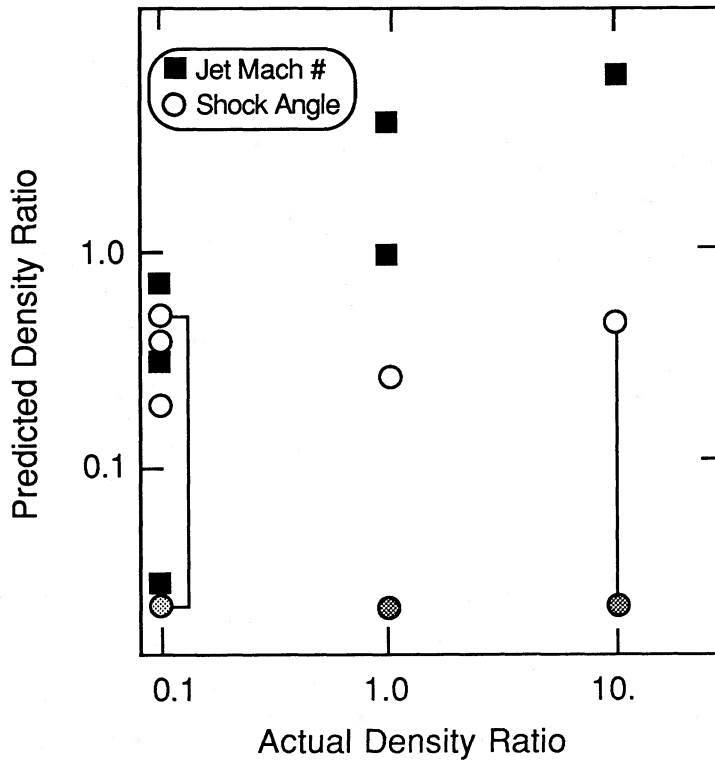

FIG. 13.—Comparison of density ratios predicted using NWS simulations and eq. (9) to the actual density ratios input by NWS. See text for definition of symbols. Shaded circles represent unphysical answers (<0) for the density ratio. Points connected by bars are two estimates from different features in the same flow simulation.

"weather" or changing conditions in the beam (e.g., Scheuer 1982; Begelman, Blandford, and Rees 1980; Williams and Gull 1985) may need to be invoked. Finally, features such as the northeast "line" may find their explanation in fundamentally asymmetric modes, such as the helical instabilities studied by Hardee (1984).

e) Ballistic Interpretation

The continuous fluid beam simulations have been used in the discussion above because they currently offer the most detail for comparison. However, many or all of the observed features of 3C 33 South may be similarly identified with aspects of the shocked fluid and wake of an intermittent beam, or even a ballistic "blob." A bow shock is, of course, created in supersonic flow around a hard object, like a blob. Likewise, the cone of synchrotron emission which trails the hot spot is similar to the laboratory wakes of hard obstacles (see, e.g., Van Dyck 1982, Figs. 259–266). The closing angle of this cone is related to the Mach number in the simplest case, but is significantly affected by the shape of the obstacle. Finally, in a ballistic model the filamentary features could be mini–bow shocks from material ablated off the main blob (W. Christiansen, private communication), or shocks driven by irregularities in the wake (see, again, Van Dyck 1982). Detailed numerical simulations are needed for blobs propagating through a fluid medium.

V. CONCLUDING REMARKS

The observation of emission downstream from the bow shock suggests that both seed particles and fields exist 100 kpc from galaxies, and that even a moderate strength shock ($M \approx 2.3$) is sufficient to accelerate the particles to sufficient energies to radiate in the radio. Furthermore, if we can use the magnetic field structure to identify the contact discontinuity, as suggested in Figure 9, then the strongest part of the hot spot comes from the highly compressed and shocked *intergalactic* medium, and *not* from the incident beam. The above conclusions assume that the relativistic plasma is tightly coupled to the thermal plasma, which is modeled in the numerical simulations. Turbulent and microscopic diffusion processes and electron streaming rates (e.g., Spangler and Basart 1981) still need to be evaluated. Finally, we need to develop reliable signatures for the identification of structures such as the contact discontinuity. Calculations of shear and compression in the numerical simulations, which would lead to predictions of magnetic field configurations, would be of substantial value.

1. The most important outcome of this work is the identification of apparent supersonic fluid flow features in the head of an extragalactic radio source, 3C 33 South, whether caused by a continuous beam or a heavy blob interacting with an intergalactic medium.

2. The head of 3C 33 South is likely to be an illuminated bow shock, which advances into the intergalactic medium at a Mach number of approximately 2.3. The synchrotron emissivity along the shock front scales with the local pressure jump as would be expected under conditions of equipartition between relativistic particles and fields.

3. Observations of both external and internal shocks in extragalactic sources may allow a determination of the underlying physical flow parameters, by comparison with numerical simulations. Significant further work is needed for this potential to be realized.

a) Final Comments

Is 3C 33 South unique or are the features shown here common in extragalactic radio sources? First, only a minority of extragalactic radio sources show a bow-shaped leading edge and transverse magnetic fields. The low value of the external Mach number, ~ 2.3, suggests that these sources may not have sufficient momentum flux per unit area to drive supersonic flow. Other sources have blunt, or multiple, or complex hot spot shapes. The connections between their morphologies and the numerical simulations are not as straightforward as in the case of 3C 33 South. Finally, should we have commonly seen the detailed underlying fluid patterns suggested here, or is the synchrotron emissivity so sensitive to precise conditions in the lobe, that others will be hard to find?

A purely observational aspect of this problem is that not enough effort has gone into looking for detailed fluid features. Without devoting substantial time in processing, and then examining the images of extragalactic radio source lobes with a flexible image processor, subtle but important details will be missed.

Anyone who is interested in examining these 3C 33 data themselves may send me a blank magnetic tape, specifying visibility data and/or maps. Paper copies of other maps (e.g., fractional polarization) not presented here are also available. Slides of these maps may be obtained from the NRAO in Charlottesville, Va.

REFERENCES

Arnold, C. 1985, Ph.D. thesis, University of Chicago.
Baars, W. J. M., Genzel, R., Pauliny-Toth, I. I. K., and Witzel, A. 1977, *Astr. Ap.*, **61**, 99.
Begelman, M. C., Blandford, R. D., and Rees, M. J. 1980, *Nature*, **287**, 307.
Bell, A. R. 1978, *M.N.R.A.S.*, **182**, 147.
Blandford, R. D., and Ostriker, J. P. 1978, *Ap. J. (Letters)*, **221**, L29.
Blandford, R. D., and Rees, M. J. 1974, *M.N.R.A.S.*, **169**, 395.
Bridle, A. H. 1982, in *IAU Symposium 97, Extragalactic Radio Sources*, ed. D. S. Heeschen and C. M. Wade (Dordrecht: Reidel), p. 121.
———. 1984, *A.J.*, **89**, 979.
Bridle, A. H., and Eilek, J. A., ed. 1984, *Physics of Energy Transport in Extragalactic Sources* (NRAO Workshop 9) (Green Bank: NRAO).

Canizares, C. 1987, in *IAU Symposium 117, Dark Matter in the Universe*, ed. J. Kormendy and G. R. Knapp (Dordrecht: Reidel), p. 165.
Clark, B. G. 1980, *Astr. Ap.*, **89**, 377.
DeYoung, D. S., and Axford, I. 1967, *Nature*, **216**, 129.
Dreher, J. W. 1981, *A.J.*, **86**, 833.
Dreher, J. W., and Simkin, S. M. 1986, *A.J.*, **91**, 58.
Eilek, J. 1979, *Ap. J.*, **230**, 373.
Fomalont, E. B. 1972, *Ap. Letters*, **12**, 187.
Hardee, P. E. 1984, *Ap. J.*, **287**, 523.
Hargrave, P. J., and McEllin, M. 1975, *M.N.R.A.S.*, **173**, 37.
Haves, P. 1975, *M.N.R.A.S.*, **173**, 553.
Henriksen, R., and Jones, T. W., ed. 1986, *Canadian J. Phys.*, **64**.

Laing, R. A. 1984, in *Physics of Energy Transport in Extragalactic Radio Sources* (NRAO Workshop 9), ed. A. H. Bridle and J. Eilek (Green Bank: NRAO), p. 90.

Matthews, T. A., Morgan, W. W., and Schmidt, M. 1964, *Ap. J.*, **140**, 35.

Meisenheimer, K., and Röser, H. J. 1986, *Nature*, **319**, 459.

Noordam, R. E., and de Bruyn, A. G. 1982, *Nature*, **299**, 597.

Norman, M. L., and Winkler, K.-H. 1985, *Los Alamos Science* (Spring/Summer 1985), p. 38.

Norman, M. L., Winkler, K.-H., and Smarr, L. 1983, in *Astrophysical Jets*, ed. A. Ferrari and A. G. Pacholcyzk (Dordrecht: Reidel), p. 227 (NWS).

———. 1984, in *The Physics of Energy Transport in Extragalactic Radio Sources* (NRAO Workshop 9), ed. A. H. Bridle and J. Eilek (Green Bank: NRAO), p. 150 (NWS).

Raga, A. C. 1986, *Ap. J.*, **308**, 829.

Reipurth, B., Bally, J., Graham, J. A., Lane, A. P., and Zealy, W. J. 1986, *Astr. Ap.*, **164**, 51.

Rudnick, L., Saslaw, W. C., Tyson, J. A., and Crane, P. 1981, *Ap. J.*, **246**, 647.

Ruzmaikan, A. A., and Sokoloff, D. D. 1977, *Astr. Ap.*, **58**, 247.

Scheuer, P. 1974, *M.N.R.A.S.*, **166**, 513.

Scheuer, P. 1982, in *IAU Symposium 97, Extragalactic Radio Sources*, ed. D. S. Heeschen and C. M. Wade (Dordrecht: Reidel), p. 163.

Schwab, F. 1980, *Proc. Soc. Photo-Opt. Instr. Eng.*, **231**, 18.

Schwartz, R. D. 1983, *Ann. Rev. Astr. Ap.*, **21**, 209.

Simkin, S. M. 1978, *Ap. J. (Letters)*, **222**, L55.

———. 1979, *Ap. J.*, **234**, 56.

Smith, M. D., Norman, M. L., Winkler, K.-H., and Smarr, L. 1985, *M.N.R.A.S.*, **214**, 67.

Spangler, S. R., and Basart, J. P. 1981, *Ap. J.*, **243**, 1103.

van Breugel, W. J. M. 1986, *Canadian J. Phys.*, **64**, 392.

van Breugel, W. J. M., and Miley, G. K. 1977, *Nature*, **265**, 315.

Van Dyck, M. 1982, *An Album of Fluid Motion* (Stanford, Ca.: The Parabolic Press).

Williams, A. G., and Gull, S. F. 1985, *Nature*, **313**, 34.

Wilson, A. S., and Ulvestad, J. 1987, *Ap. J.*, **319**, 105.

Wilson, M. J., and Scheuer, P. A. G. 1983, *M.N.R.A.S.*, **205**, 449.

Woodward, P. R. 1986, in *Astrophysical Radiation Hydrodynamics*, ed. K.-H. Winkler and M. L. Norman (Dordrecht: Reidel) p. 245.

LAWRENCE RUDNICK: University of Minnesota, Department of Astronomy, School of Physics and Astronomy, 116 Church Street SE, Minneapolis, MN 55455